The Cryosphere Discuss., 8, 2685–2719, 2014
www.the-cryosphere-discuss.net/8/2685/2014/
doi:10.5194/tcd-8-2685-2014

The Cryosphere Discussions
Open Access

Destabilisation of an Arctic ice cap triggered by a hydro-thermodynamic feedback to summer-melt

T. Dunse[1], T. Schellenberger[1], A. Kääb[1], J. O. Hagen[1], T. V. Schuler[1], and C. H. Reijmer[2]

[1]Department of Geosciences, University of Oslo, P.O. Box 1047, Blindern, 0316 Oslo, Norway
[2]Institute for Marine and Atmospheric Research Utrecht, Utrecht University, Princetonplein 5, 3584 CC Utrecht, the Netherlands

Received: 14 April 2014 – Accepted: 8 May 2014 – Published: 23 May 2014

Correspondence to: T. Dunse (thorben.dunse@geo.uio.no)

Published by Copernicus Publications on behalf of the European Geosciences Union.

Abstract

Mass loss from glaciers and ice sheets currently accounts for two-thirds of the observed global sea-level rise and has accelerated since the 1990s, coincident with strong atmospheric warming in the Polar Regions. Here we present continuous GPS measurements and satellite synthetic aperture radar based velocity maps from the Austfonna ice cap, Svalbard, that demonstrate strong links between surface-melt and multiannual ice-flow acceleration. We identify a hydro-thermodynamic feedback that successively mobilizes stagnant ice regions, initially frozen to their bed, thereby facilitating fast basal motion over an expanding area. By autumn 2012, successive destabilization of the marine terminus escalated in a surge of the ice cap's largest drainage basin, Basin-3. The resulting iceberg discharge of $4.2 \pm 1.6\,\mathrm{Gt\,a^{-1}}$ over the period April 2012 to May 2013 triples the calving loss from the entire ice cap. After accounting for the terminus advance, the related sea-level rise contribution of $7.2 \pm 2.6\,\mathrm{Gt\,a^{-1}}$ matches the recent annual ice-mass loss from the entire Svalbard archipelago. Our study highlights the importance of dynamic glacier wastage and illuminates mechanisms that may trigger a sustained increase in dynamic glacier wastage or the disintegration of ice-sheets in response to climate warming, which is acknowledged but not quantified in global projections of sea-level rise.

1 Introduction

Glacier mass loss constitutes the largest contributor to global mean sea-level rise (SLR), followed by ocean thermal expansion (Church et al., 2011). Over the last two decades, not only the glaciers and ice caps (Kaser et al., 2006), but also the ice sheets have lost mass at accelerating rates (AMAP, 2011; Shepherd et al., 2012). These ice mass changes coincide with atmospheric warming that causes record summer temperatures and glacier melt in the Arctic (Gardner et al., 2011) and across the Greenland ice sheet (Tedesco et al., 2013). Recently, the West Antarctic ice sheet has been

TCD
8, 2685–2719, 2014

reported as one of the world's fastest warming regions (Bromwich et al., 2013). In addition to mass loss by melting, glacier dynamics have the potential to significantly amplify glacier response to climate change by altering the ice discharge to the ocean. Outlet-glacier, respectively ice-stream acceleration is generally attributed to hydraulic lubrication and oceanic-warming induced destabilization of floating ice tongues in the case of the Greenland ice sheet and reduced buttressing by thinning or loss of ice shelves in the case of the West Antarctic ice sheet (WAIS) (Shepherd et al., 2012). Recent observations of sustained ice flow and mass loss from Northeast Greenland and West Antarctica are also reported as evidence of a marine ice-sheet instability (Khan et al., 2014; Mouginot et al., 2014). The phenomenon, also known as tidewater-glacier instability, refers to glacier speed-up due to terminus retreat into deeper water (Meier and Post, 1987; Pfeffer, 2007).

To date, glacier-dynamic feedback processes remain poorly constrained and are therefore not yet incorporated in global projections of future glacier wastage (Stocker et al., 2013). SLR projections released with the IPCC Fifth Assessment Report range from 0.26 to 0.82 m over the 21st century (Stocker et al., 2013). The projections include ice discharge from the ice sheets into the ocean, however, based on current discharge rates and not accounting for a future dynamic response to climate change. The IPCC acknowledges, but is not able to quantify the probability of significantly higher SLR, such as associated with disintegration of marine-based sectors of the Antarctic ice sheet (Stocker et al., 2013). Rapid marine ice-sheet disintegration is evident from geological records both in the Northern and Southern Hemisphere and typically associated with air temperatures similar or warmer than those predicted for the end of the 21st century (Cook et al., 2013; Deschamps et al., 2012). Ice-rafted debris distributed across the North Atlantic ocean floor provide evidence of substantial calving associated with the rapid disintegration of the Laurentide ice sheet, so-called Heinrich events (Bond et al., 1992). Paleoclimatic records suggest rates of sea-level change much larger than currently observed or projected for the 21st century, e.g. 3.5 to 5 m

TCD
8, 2685–2719, 2014

SLR per century (35–50 mm a^{-1}) at the end of the last glacial maximum, ~ 14.5 ka ago (Deschamps et al., 2012).

Variations in glacier flow and hence ice discharge, encompass wide ranges of timescales and magnitudes, from diurnal velocity fluctuations to century-scale surge-type behaviour, and are mainly attributed to changes in basal drag (Clarke, 1987). Seasonal velocity variations are externally controlled by surface-melt induced acceleration through basal lubrication (Bindschadler, 1983). The rate of water supply to the glacier bed and the capacity of the subglacial drainage system to accommodate increased discharge regulate the basal water pressure and therewith basal drag (Schoof, 2010). Increased meltwater supply may thus accelerate, but also slow down ice flow, if it facilitates the establishment of a hydraulically efficient drainage system (Schoof, 2010). Several recent studies therefore suggest that hydraulic lubrication alone has a more limited effect on the future net mass balance of the Greenland ice sheet (Nick et al., 2013; Shannon et al., 2013) than previously anticipated (Zwally et al., 2002). However, these assessments do not account for changes in the extent of the basal area subjected to hydraulic lubrication (Nick et al., 2013) or the associated calving loss (Shannon et al., 2013). The effect of surface meltwater on the thermal structure of glaciers has only recently been considered in modelling studies (Phillips et al., 2010). The process of latent heat release and direct heat transfer from water in glaciers was termed cryo-hydrological warming (Phillips et al., 2010). Cryo-hydrological warming has the potential to change englacial and basal temperatures within years, whereas changes in the basal thermal regime by heat conduction would require decades to centuries (Phillips et al., 2010). Present outlet glaciers may accelerate significantly, if meltwater drainage to the bed would spread inland and thaw areas of the bed that are currently frozen (Alley et al., 2008). We propose that cryo-hydrological warming may have a drastic effect on glacier dynamics by weakening cold-based marginal ice regions that obstruct outflow of inland ice regions with basal temperatures already at or near the pressure melting point.

TCD
8, 2685–2719, 2014

Cyclic surge-type behaviour is an extreme example of variations in glacier flow and characterized by long quiescent phases (decades to centuries) with slow flow velocities followed by short-lived active phases (months to years) with orders-of-magnitude increases in flow velocities (Raymond, 1987). During a surge, mass is transferred from an upper reservoir area to a lower receiving area, often associated with kilometre-scale advances of the terminus and greatly enhanced calving flux, in the case of tidewater glaciers. A thermally controlled soft-bed surge mechanism has been proposed for the polythermal glaciers of Svalbard (Hamilton and Dowdeswell, 1996). When thawed, unconsolidated, water-saturated sediments lack shear strength and have the potential to efficiently destabilize the overlying ice (Tulaczyk et al., 2000). Surge-type behaviour is generally considered independent of climatic forcing. Internal mechanisms may be sufficient to drive cyclic instabilities (MacAyeal, 1993). Changes in glacier geometry during the quiescent phase provoke corresponding changes in driving stress and basal thermal regime (Clarke, 1976). Nevertheless, the climatic mass balance influences the build-up of the reservoir area and therewith the surge periodicity. In addition, external factors drive feedback processes that lead to amplified dynamic response, pushing the glacier towards an instability threshold.

Here we present observations of multiannual ice-stream acceleration of a large Arctic ice cap, culminating in a surge and drastically enhanced ice discharge. Our observations demonstrate strong links between surface-melt and ice-flow acceleration. We propose a hydro-thermodynamic feedback that efficiently weakens the basal drag in initially frozen areas and facilitates enhanced basal motion over an expanding temperate basal area. By identifying the hydro-thermodynamic feedback to summer melt as a trigger for the mobilization of initially slow-moving ice regions, our study contributes to the understanding of dynamic glacier wastage and disintegration mechanisms of the ice-sheets in a warming climate (Alley et al., 2008; Joughin and Alley, 2011), i.e. characterized by more widespread and intense occurrence of surface melt.

TCD
8, 2685–2719, 2014

2 Austfonna, Basin-3

At ∼ 7800 km^2, Austfonna is the largest ice cap in the Eurasian Arctic (Fig. 1a). The ice cap consists of a main dome with an ice thickness of up to 600 m that feeds a number of drainage basins, some of them known to have surged in the past (Lefauconnier and Hagen, 1991). Austfonna has a polythermal structure. In the ice cap's interior basal temperatures are likely at pressure melting point (Zagorodnov et al., 1989), while the thinner ice-cap margins are cold and frozen to the ground, except for distinct fast flowing outlets that are dominated by fast basal motion and intersperse the generally slowly deforming ice cap (Dowdeswell et al., 1999). The south-eastern basins are to a large extent grounded below sea level, and form a continuous, non-floating calving front towards the Barents Sea (Dowdeswell et al., 2008). The regions grounded below sea level are to some extent underlain by marine sediments (Dowdeswell et al., 2008). Over 2002–2008, the climatic mass balance of Austfonna was close to zero (Moholdt et al., 2010a). Yet, the ice cap was losing mass due to calving and retreat of the marine ice margin that accounted for 2.5 Gt a^{-1} or 33 ± 5 % of the total ablation (Dowdeswell et al., 2008).

Basin-3 (∼ 1200 km^2) is the largest drainage basin of Austfonna and topographically constrained by a subglacial valley that extends from south of the main dome eastwards towards the Barents Sea (Fig. 1b). About one third of the ice base is grounded below sea level down to a maximum depth of ∼ 155 m within an overdeepening in the central terminus region. A previous velocity map based on interferometric SAR data acquired in the mid-1990s revealed an ice stream in the northern lower reaches of Basin-3 with flow velocities ≤ 200 m a^{-1} (Dowdeswell et al., 2008). The ice stream was topographically constrained by a subglacial mountain to the north (Isdomen) and near-stagnant ice, likely frozen to its bed, to the south. The absence of surface lineation (e.g. crevasses) as late as 1991, identified the ice stream of Basin-3 as a recent feature (Dowdeswell et al., 1999). During the 1990s, the front retreated on average by 70 ± 10 m a^{-1}, accounting for two thirds of the calving flux of ∼ 0.4 Gt a^{-1} (Dowdeswell

TCD
8, 2685–2719, 2014

et al., 2008). Basin-3 is known to have surged some years prior to 1870 (Lefauconnier and Hagen, 1991), and the advancing terminus created a pronounced surge lobe nearly 25 km in width. The terminal moraine associated with the last surge lies ~ 8 km from the present-day position of the calving front (Robinson and Dowdeswell, 2011). Based on lobe volume and accumulation rate, the duration of the quiescent phase has been estimated to last 200–500 years (Dowdeswell et al., 1991).

3 Methods

3.1 GPS velocity timeseries

In spring 2008, five GPS receivers were deployed along the mid-1990's central flowline, 5 to 16 km upglacier from the calving front (Fig. 1; Dunse et al., 2012). We used GPS single-frequency code receivers (L1 band). Geographical positions were logged at hourly intervals, every third hour for instruments installed after May 2011, at an accuracy typically better than 2 m (den Ouden et al., 2010). Filtering in the time domain was applied to reduce random errors, i.e. a 7-day running mean was applied to the daily mean position, velocities were computed, and finally, the velocity was smoothed by applying another 7-day running mean (Dunse et al., 2012).

3.2 Velocity maps from synthetic aperture radar

Velocity maps of Basin-3, Austfonna, were produced from 20 2 m resolution TerraSAR-X (TSX) scenes acquired between April 2012 and May 2013, and provided by the German Aerospace Center (DLR). Displacement fields were derived by using cross correlation between two consecutive acquisitions (Strozzi et al., 2002) and geocoded using a DEM of Austfonna (Moholdt and Kääb, 2012). Appendix A provides more detailed information on the TSX data and processing. Calving front outlines were digitized from geocoded backscatter images (Appendix B). The calving flux of Basin-3

TCD
8, 2685–2719, 2014

was derived by the ice flux through a fixed fluxgate upglacier of the calving front and the area change downglacier of that fluxgate, multiplied by an average ice thickness.

3.3 Additional data

To approximate timing and magnitude of surface-melt periods, cumulative positive-degree days (PDD) were computed from the temperature record of an automatic weather station. The station was operated since April 2004 on the western flank of Austfonna at 22°25′12″ E, 79°43′48″ N and 370 m a.s.l. (Schuler et al., 2014). Surface crevasses were identified and mapped using ground-penetrating radar (Ramac GPR; Målå Geoscience) at a centre frequency of 800 MHZ, providing structural information from the glacier surface down to a depth of ∼ 12 m (Dunse et al., 2009, Appendix C). GPR profiles were annually repeated since 2004 and geolocated using a kinematic Global Navigation Satellite System (GNSS; GPS and GLONASS).

4 Results

4.1 Multi-annual ice-flow acceleration

In spring 2008, five GPS receivers were deployed along the mid-1990's central flowline, 5 to 16 km upglacier from the calving front (Fig. 1; Dunse et al., 2012). Winter velocities observed in May 2008, were significantly higher than in the mid-1990s (Fig. 2). The GPS time series also reveal considerable overall acceleration, occurring in pronounced steps, each of which coincides with the summer melt period, as indicated by the temperature record of an automatic weather station (Fig. 2; Schuler et al., 2014). High sensitivity and short response time (days) of glacier dynamics to melt periods clearly suggest surface-melt triggered acceleration. The 2008 summer speed-up is followed by a gradual winter deceleration, returning to pre-summer velocities only before the onset of the 2009 summer speed-up (maximum not captured due to instrument-power loss). However, during subsequent years, the summer speed-ups were progressively

TCD
8, 2685–2719, 2014

irreversible, resulting in elevated winter velocities (Appendix D, Fig. 8). In autumn 2012, strong acceleration continued although surface melt had ceased.

4.2 Mobilization of stagnant ice regions

The drastic acceleration during autumn 2012 coincided with the expansion of the fast-flowing region across the entire basin, as revealed by a time series of ice-surface velocity maps based on intensity tracking of repeat-pass TerraSAR-X satellite radar images (Fig. 3; Appendix B). Ice-stream velocities in April 2012 were up to $3\,\mathrm{m\,d^{-1}}$, one order of magnitude larger than in the mid 1990's (Fig. 3a). In April 2012, the ice stream extended further inland and had widened southward to a width of $\sim$6–8 km, as compared to $\sim$5–6 km in the mid-1990s. Consequently, the GPS receivers were located $\sim$1 km north from the central flowline and did not capture fastest flow velocities. In contrast to the mid-1990s, the south-eastern corner of Basin-3 displayed also fast motion, at velocities of up to $1\,\mathrm{m\,d^{-1}}$. These two distinct fast-flow regions were completely separated by almost stagnant ice, notably including the calving front. Low ice velocities, $<0.1\,\mathrm{m\,d^{-1}}$, indicate the absence of considerable basal motion, and suggest frozen-bed conditions in this region. In August 2012, i.e. at the end of the summer melt season, velocities had increased significantly, up to $6\,\mathrm{m\,d^{-1}}$ for the northern and $4\,\mathrm{m\,d^{-1}}$ for the south-eastern fast-flow region, along with further lateral expansion of the fast flowing areas. Consequently, the slow moving ice region in-between had decreased in size (Fig. 3b) and disappeared by October 2012, when ice flow escalated into a surge comprising the entire width of the basin, reaching velocities $>10\,\mathrm{m\,d^{-1}}$ (Fig. 3c). Velocities increased further until January 2013, reaching a maximum of $20\,\mathrm{m\,d^{-1}}$ (Fig. 3d; Table 2). Between January and May 2013 the maximum velocities decreased to $15.2\,\mathrm{m\,d^{-1}}$, while the upglacier regions continued to accelerate (Fig. 5b). By the end of 2013, fast flow of Basin-3 continued (Table 2).

TCD
8, 2685–2719, 2014

4.3 Calving flux

The TSX data allowed calculation of the calving flux components, i.e. (i) the ice flux through a fixed fluxgate near the calving front, and (ii) the mass change of the terminus downglacier of that fluxgate, accounting for front position changes (Fig. 4; Appendix B). The observed ice flux peaked at a rate of $13.0 \pm 4.2\,\mathrm{Gt\,a^{-1}}$ in December 2012/January 2013, after which it decreased slightly (Fig. 4a). Prior to October 2012, the position of the entire calving front of Basin-3 was remarkably stable (slight retreat; Fig. 4b), indicating that the entire ice flux was balanced by iceberg calving. After November 2012, the southern and central parts of the front, advanced by >1 km, reducing ice mass loss through calving by 61 %, as opposed to a stable front position.

Direct conversion of calving mass loss to SLR contribution is only meaningful for a static calving front. Glacier surges are typically accompanied by significant terminus advances. An advancing terminus reduces the mass loss from the glacier, however, the submerged part of the terminus replaces sea water instantaneously, causing an instantaneous sea-level rise. We therefore distinguish between a glacier-mass balance and a sea-level perspective on the calving flux (Table 1; Fig. 4c). From 19 April 2012 to 9 May 2013, calving mass loss [yearly rate] from Basin-3 accounted for $4.4 \pm 1.6\,\mathrm{Gt\,a^{-1}}$ [$4.2 \pm 1.6\,\mathrm{Gt\,a^{-1}}$], an order of magnitude increase compared to 1991–2008 (Dowdeswell et al., 2008), nearly tripling the calving loss from the entire Austfonna ice cap. The related sea-level rise contribution of $7.6 \pm 2.7\,\mathrm{Gt\,a^{-1}}$ [$7.2 \pm 2.6\,\mathrm{Gt\,a^{-1}}$], is as large as the total glacier mass change from the entire Svalbard archipelago for the period 2003 to 2008, estimated to $-6.6 \pm 2.6\,\mathrm{Gt\,a^{-1}}$ (Moholdt et al., 2010b).

5 Discussion of hydro-thermodynamic feedback mechanism

The dynamic changes that have been observed at Basin-3 over the last two decades can be separated into three phases: (1) activation of a spatially confined ice stream in the early 1990's (Dowdeswell et al., 1999); (2) multi-annual acceleration from < 2008

TCD
8, 2685–2719, 2014

to 2012, along with an expansion of the ice stream; (3) active surge phase following the destabilization of the entire terminus in autumn 2012.

The activation of a spatial confined ice stream in the early 1990's (phase 1) can be explained by internal mechanisms, e.g. gradual changes in basal thermal regime and driving stress (Dunse et al., 2011), following the geometric build-up of the glacier over ~ 120 years of quiescence. The multi-annual, stepwise acceleration in the prelude of the present surge (phase 2, observed by GPS since 2008) coincides with successive annual summer speed-ups (Fig. 2). Short-lived acceleration during the melt season is consistent with current understanding of hydraulic lubrication (Schoof, 2010). In contrast, the multi-annual acceleration of background velocities (Fig. 8) cannot be explained by this mechanism and suggests a fundamental change in dynamics. Enhanced post-summer velocities sustained throughout the winter can be explained by successive activation of previously stagnant ice regions during the previous summer melt period. Mobilization of increased ice volumes within the reservoir area lead to increased ice-stream velocities and discharge. A widening of the ice stream itself, allows for higher centre-line velocities due to the increased distance from the lateral shear margin (Joughin and Alley, 2011).

Mobilization of the reservoir area is evident from the surface-crevasse formation within the upper accumulation area of Basin-3. Ground-penetrating radar (GPR) surveys reveal first occurrence of surface crevasses from ~ 2004 onwards (Appendix C; Fig. 7). Crevasses are a manifestation of longitudinal extension and evidence of upglacier migration of the fast-flowing region. This is in line with the upglacier expansion of the ice stream revealed by TSX and the annual position change of a mass-balance stake close to the ice divide (Fig. 1), subjected to strong acceleration from 11 m a^{-1} between 2004 and 2007 to 28, 43 and 114 m a^{-1} for the period 2010–2013. The first occurrence of crevasses signify the development of potential meltwater routes to the glacier bed, subjecting an increasing region to hydraulic basal lubrication and cryo-hydrologic warming. Similarly, meltwater reaching the bed beneath the heavily crevassed shear margin efficiently weakens the basal drag that balances the lateral

TCD
8, 2685–2719, 2014

drag, which in turn regulates ice stream velocities (Joughin and Alley, 2011). Cryo-hydrologic warming and increased frictional heating both act to enhance this positive feedback, weakening the flow resistance exerted by the lateral shear margins and initially cold-based ice patches acting as "sticky spots". The interplay between cryo-hydrologic warming and the emergence of basal hydraulic lubrication over an expanding area of the ice base constitutes a hydro-thermodynamic feedback. Unconsolidated subglacial sediments underneath the marine-based ice of Basin-3 would act to further enhance this feedback, and when thawed, favour rapid destabilization (Hamilton and Dowdeswell, 1996; Tulaczyk et al., 2000).

A surge comprising the full width of Basin-3 and the subsequent advance of the terminus followed the mobilization of the remaining slow moving regions, notably including the calving front (phase 3). The abrupt onset of fast flow suggests sheer tearing of the glacier from its bed, after the remaining sticky spots have been sufficiently weakened by the hydro-thermodynamic feedback outlined above. While fast flow continued by the end of 2013, it is expected to slow down or come to a halt within a few years. Massive ice redistribution from the reservoir into the receiving area and towards the calving front efficiently lowers the driving stress. Eventually, temperate basal conditions underneath the dynamically thinned and decelerating terminus are expected to be no longer maintained, at which time the base of the ice will start to refreeze to its bed (Dunse et al., 2011).

To what extent can present dynamics of an Arctic ice cap like Austfonna shed light on the future dynamic behaviour of ice sheets? Analogue to the ice sheets, Austfonna consist of slow moving inland ice interspersed by faster flowing outlet glaciers and ice streams that deliver inland ice towards the calving front. Drainage basins in their quiescent phase are characterized by margins frozen to their bed (Dowdeswell et al., 1999). Similarly, the coastal margins of the Antarctic ice sheet contain large regions of cold-based ice (Pattyn, 2010) that may currently prohibit efficient drainage of warm-based interior ice towards the ocean – e.g. in the Wilkes Basin, East Antarctica, that is known to have been dynamically active during the Pliocene warmth (Cook et al.,

TCD
8, 2685–2719, 2014

2013). In southwest Greenland, further acceleration of Jacobshavn Isbræ followed the 2012 record summer melt season (Joughin et al., 2014). Although the authors attribute the acceleration to terminus retreat into a bedrock depression, the occurrence of pronounced summer speed up at higher elevations may also reflect inland migration of surface melt and the effect of associated hydraulic feedbacks on glacier dynamics (Alley et al., 2008; Meierbachtol et al., 2013; Phillips et al., 2013). Similarly, the hydro-thermodynamic feedback may play a role in the sustained mass loss recently reported from northeast Greenland and mainly attributed to sea-ice decline due to regional waming (Khan et al., 2014).

6 Summary and conclusion

Our observations of multiannual acceleration of an Arctic ice cap indicate successive enhancement of basal motion driven by meltwater supply and shed light on a destabilisation mechanisms of Polar land ice. We propose a hydro-thermodynamic feedback mechanism, triggered by surface melt reaching a growing fraction of the glacier bed. Intrusion of surface melt to the glacier bed provides an efficient heat source through cryo-hydrological warming and initiates hydraulic lubrication, weakening the resistance to basal motion, especially in initially cold-based ice regions. During the summer melt season, slow moving ice regions are successively mobilized through lateral and inland expansion of regions dominated by fast basal motion.

The recent calving flux of Basin-3 is enormous and has strong implications for the mass balance of the ice cap and its contribution to sea-level rise. From 19 April 2012 to 9 May 2013, the calving flux [yearly rate] of Basin-3 amounted to $4.4 \pm 1.6\,\mathrm{Gt\,a^{-1}}$ [$4.2 \pm 1.6\,\mathrm{Gt\,a^{-1}}$], an order of magnitude increase compared to 1991–2008 (Dowdeswell et al., 2008). Accounting for the terminus advance, the related sea-level rise contribution of $7.6 \pm 2.7\,\mathrm{Gt\,a^{-1}}$ [$7.2 \pm 2.6\,\mathrm{Gt\,a^{-1}}$] equals the total annual glacier-mass loss from the entire Svalbard archipelago for the period 2003 to 2008, estimated to $6.6 \pm 2.6\,\mathrm{Gt\,a^{-1}}$ (Moholdt et al., 2010b).

TCD
8, 2685–2719, 2014

Given continued climatic warming, we hypothesize that the hydro-thermodynamic feedback to surface melt will gain significance for the destabilisation of Polar land ice, including the ice sheets. In light of recent record melt and rising ELA of the Greenland Ice Sheet, the proposed mechanism has the potential to lead to a long-term enhancement of outlet-glacier discharge and calving loss. Our expectation contrasts recent studies that indicate limited effects of surface-melt induced acceleration on the future net-mass balance of the Greenland ice Sheet (Nick et al., 2013; Shannon et al., 2013). Surface melt in Antarctica is presently mainly constrained to the ice shelves (Comiso, 2000). Given strong continued warming, surface melt will increasingly occur over coastal areas of Antarctica, making the grounded ice-sheet margins vulnerable to the hydro-thermodynamic feedback. Our study of the Austfonna ice cap highlights the importance of dynamic glacier wastage for the mass balance of Polar land ice. Current model projections of future SLR (Stocker et al., 2013) still do not account for the dynamic response of glaciers to continued global warming and might need to be revised upward after incorporating mechanisms such as the hydro-thermodynamic feedback.

Appendix A: TerraSAR-X velocity maps

20 TerraSAR-X (TSX) satellite synthetic aperture radar scenes of ~ 2 m ground resolution (TSX Stripmap mode) were acquired between April 2012 and December 2013 (Table 2), providing information on the spatial evolution of the surge (Fig. 3). For each pair of consecutive acquisitions, displacements were determined using cross-correlation of the intensity images (Strozzi et al., 2002) and 19 velocity maps produced by accounting for the respective repeat-pass period (Table 2). The size of the matching-window was adjusted according to the expected maximum displacements during the repeat pass cycle, 300 × 344 pixels in range and azimuth direction in case of 11 days or 599 × 688 pixels for 22 days or longer. Displacements were measured in discrete steps of 50 × 57 pixels in range and azimuth to achieve a resolution of ~ 100 × 100 m. Velocity maps were calculated from displacement maps by accounting for the time interval between

TCD
8, 2685–2719, 2014

the two underlying TSX images (t_1 to t_{19}, Table 2) and geocoded using a DEM of Austfonna (Moholdt and Kääb, 2012). Velocities larger than a carefully estimated maximum (Table 2) were classified as mismatches and removed. To estimate the ice flux (Appendix B), obvious erroneous velocities remaining in the vicinity of a fixed fluxgate were manually removed and the maps interpolated using inverse distance weighting to provide continuous velocity profiles along the fluxgate (Fig. 5a). A comparison between TSX and GPS velocities for each GPS station and all repeat-pass periods, revealed that TSX underestimated local velocities at the GPS stations by 0.3 m d^{-1} (Fig. 6). We explain this small bias by large horizontal velocity gradients within large matching windows, which could lead to the average velocities within a matching window being typically smaller than the strictly local GPS velocity. Consequently, more stable areas produce best matches.

Appendix B: Calving flux

The calving flux, q, of Basin-3 was calculated based on TSX velocity maps and changes in extend of the glacier by $q = q_{fg} + q_t$, with q_{fg} being the ice flux through a fluxgate near the calving front, and q_t the volume change of the terminus downglacier of that fluxgate due to advance or retreat of the calving front. Here, we defined a spatially fixed fluxgate approximately perpendicular to the ice flow, typically 1–3 km upglacier from the actual calving front (Fig. 5a), and where ice surface velocities could be inferred from all TSX-image pairs. The ice-flux can be written as

$$q_{fg} = H_{fg} \cdot w_{fg} \cdot v_{fg}$$

where $H_{fg} = zs_{fg} - zb_{fg}$ is the ice thickness along the fluxgate, with zs_{fg} and zb_{fg} surface and bedrock elevation, respectively, w_{fg} is the width of the fluxgate and v_{fg} the velocity across the fluxgate. We assume plug flow, i.e. depth averaged velocities equal surface velocities, because at the high flow velocities observed, ice deformation is negligible compared to basal motion (Clarke, 1987). Position changes of the calving front are

TCD
8, 2685–2719, 2014

addressed by changes in areal extent of the glacier downstream from that fluxgate per repeat-pass period

$$q_t = H_t \cdot \frac{\Delta A_t}{\Delta t}$$

where $H_t = zs_t - zb_t$ is the ice thickness at the terminus in vicinity of the calving front, where zs_t represents a typical height of the calving front and zb_t is the mean bedrock elevation for the area encompassed by the observed maximum and minimum glacier extent. ΔA_t is the areal change of the terminus over the repeat-pass period Δt between successive TSX acquisitions. The uncertainty in the calving flux estimate is associated with uncertainties of the input variables listed in Table 3. If the variables are derived from several independent components, their uncertainties can be summed by the root of the sum of squares (RSS) of the uncertainty of the components.

B1 Ice flux

To calculate the ice flux $q_{\mathrm{fg},i}$ for each repeat pass period t_i (Fig. 4a), the ice flux through 617, 50 m-wide fluxgate segments was integrated, accounting for local ice thickness and velocity. Ice volume is converted to mass using an ice density $\rho_{\mathrm{ice}} = 917\,\mathrm{kg\,m^{-3}}$. The cumulative ice flux over the period 19 April 2012 to 9 May 2013 is derived by summing up the ice flux over 19 successive TSX repeat-pass periods, weighted by their time duration (Fig. 4b),

$$q_{\mathrm{fg}} = w_{\mathrm{fg}} \cdot \sum_{t_i=1}^{19} \sum_{n=1}^{617} H|_{\mathrm{fg},n} \cdot v|_{\mathrm{fg},i,n} \cdot \rho_{\mathrm{ice}}$$

To derive continuous velocity profiles along the fluxgates, the velocity maps were interpolated horizontally in the vicinity of the fluxgate where mismatches occurred. The velocity maps associated with long repeat pass periods, t_3 and t_6, suffer from large gaps, only 51 and 46 % of the fluxgate segments hold sound velocity estimates. In

TCD
8, 2685–2719, 2014

case of t_3, the available data aligns with the previous velocity profile for t_2, a factor x relation was determined and the gaps filled by piecewise polynomial interpolation so that $v(t_3) = x \cdot v(t_2)$. In case of t_6, the velocity profile was constructed by using the mean of the previous and following repeat-pass cycle, $v(t_6) = \frac{1}{2} \cdot (v(t_5) + v(t_7))$ (dash-dotted lines in Fig. 5a). The accuracy of the resulting velocity profiles were evaluated by comparing the constructed velocity profiles and the available reliable matches, revealing a standard deviation of 0.21 and 0.25 m d^{-1} and a negligible mean offset of 0.03 and 0.04 m d^{-1}, in case of t_3 and t_6, respectively.

The uncertainty in the ice-flux term, Δq_{fg}, is derived according to the law of propagation of uncertainty

$$\Delta q_{\mathrm{fg}} = w_{\mathrm{fg}} \cdot \sum_{t_i=1}^{19} \sum_{n=1}^{617} \sigma(q_{\mathrm{fg}})_{i,n}$$

with $\left(\frac{\sigma(q_{\mathrm{fg}})}{q_{\mathrm{fg}}}\right)^2 = \left(\frac{\sigma(H_{\mathrm{fg}})}{H_{\mathrm{fg}}}\right)^2 + \left(\frac{\sigma(v_{\mathrm{fg}})}{v_{\mathrm{fg}}}\right)^2$, omitting indexes i and n.

B2 Position changes of calving front

Similarly, the calving-flux term related to position changes of the calving front can be expressed by the volume change of the terminus in vicinity of the calving front, q_{t}:

$$q_{\mathrm{t}} = H_{\mathrm{t}} \cdot \sum_{t_i=1}^{19} \frac{\Delta A_{t,i}}{\Delta t_i} \cdot \rho_{\mathrm{ice}}$$

The calving front outlines of Basin-3 were digitized from geocoded TSX intensity images. Due to layover and shadow effects along the calving front a systematic error in the order of twice the height of the calving front of 30 m is assumed (Moholdt and Kääb, 2012). The digitizing accuracy is conservatively estimated to 4 pixels, i.e. ±8 m.

TCD
8, 2685–2719, 2014

Analog to the ice-flux term, the uncertainty in the terminus-change term, Δq_t, is determined by the law of propagation of uncertainty:

$$\Delta q_t = \sum_{t_i=1}^{19} \sigma(q_t)_i \cdot \rho_{ice}$$

For each repeat-pass period $\sigma(q_t)$ is determined by $\left(\frac{\sigma(q_t)}{q_t}\right)^2 = \left(\frac{\sigma(H_t)}{H_t}\right)^2 + \left(\frac{\sigma(\Delta A_t)}{\Delta A_t}\right)^2$, omitting index i.

Appendix C: Crevasse formation

Ground-penetrating radar (GPR) profiling was performed on Austfonna on an annual basis since spring 2004 (Dunse et al., 2009). The GPR was operated at a centre frequency of 800 MHZ and provides information over a depth range of about ~ 12 m. The data allows for identification of individual surface crevasses. Survey profiles initially focused on the accumulation area. Since 2008, also the flowline along which GPS receivers are deployed, was repeatedly surveyed. In the accumulation area, crevasse formation took place between 2004 and 2007 (Fig. 7a and b) and 2008 and 2012 (Fig. 7c and d), for the western and eastern profile, respectively. The monitored flowline towards the terminus was already heavily crevassed at the time of the first GPR survey (Fig. 7c).

Appendix D: Background GPS velocities and summer speed-up

Our five-year GPS record from Basin-3 shows that the annual velocity minimum typically occurs in June, just prior to the onset of summer speed-up (Dunse et al., 2012). Since 2008, the mean velocity in June has increased dramatically, with values in 2012 3 to 5 times higher than in 2008 at lowest (GPS B3 #1) and highest elevation (B3 #5),

TCD
8, 2685–2719, 2014

respectively (Fig. 8a and b). The strong acceleration results from flow velocities remaining above their pre-summer values after the annual summer speed-up. In particular, the reversible fraction of the summer speed-up decreases with time and diminishes in 2013, when the entire basin is surging (Fig. 8c). While the two upper GPS stations (B3 #4 and B3 #5) experience further drastic acceleration (factor 24 and 18 increase in June 2013 compared to June 2008, respectively), the lower GPS stations (B3 #1 and B3 #2) only show moderate velocity increases, because the locations are close to the lateral shear margins of the surging basin (Fig. 3c and d).

Acknowledgements. T.D. thanks T. Eiken and G. Moholdt for assistance in the field, W. Boot for construction of GPS receivers and C. Nuth for discussions around the manuscript. A.K. and T.S. thank DLR for provision of TSX-data (LAN_0211). This study was supported by the European Union 7th Framework Programme through the project ice2sea, grant number 226375, the Norwegian Space Centre/European Space Agency (ESA) through CryoVEx, the Research Council of Norway through CRYOMET, grant number 214465 and RASTAR, grant number 208013.

References

Alley, R. B., Fahnestock, M., and Joughin, I.: Climate change. Understanding glacier flow in changing times, Science, 322, 1061–1062, doi:10.1126/science.1166366, 2008. 2688, 2689, 2697

AMAP: Snow, Water, Ice, Permafrost in the Arctic (SWIPA): Climate Change and the Cryosphere, vol. XII, Arctic Monitoring and Assessment Programme (AMAP), Oslo, Norway, 2011. 2686

Bindschadler, R.: The importance of pressurized subglacial water in separation and sliding at the glacier bed, J. Glaciol., 29, 3–19, 1983. 2688

Bond, G., Heinrich, H., Broecker, W., Labeyrie, L., McManus, J., Andrews, J., Huon, S., Jantschik, R., Clasen, S., Simet, C., Tedesco, K., M., K., Bonani, G., and Ivy, S.: Evidence for massive discharges of icebergs into the North-Atlantic ocean during the last glacial period, Nature, 360, 245–249, 1992. 2687

TCD
8, 2685–2719, 2014

Bromwich, D. H., Nicolas, J. P., Monaghan, A. J., Lazzara, M. A., Keller, L. M., Weidner, G. A., and Wilson, A. B.: Central West Antarctica among the most rapidly warming regions on Earth, Nat. Geosci., 6, 139–145, doi:10.1038/ngeo1671, 2013. 2687

Church, J. A., White, N. J., Konikow, L. F., Domingues, C. M., Cogley, J. G., Rignot, E., Gregory, J. M., van den Broeke, M. R., Monaghan, A. J., and Velicogna, I.: Revisiting the Earth's sea-level and energy budgets from 1961 to 2008, Geophys. Res. Lett., 38, L18601, doi:10.1029/2011GL048794, 2011. 2686

Clarke, G.: Thermal regulation of glacier surging, J. Glaciol., 16, 231–250, 1976. 2689

Clarke, G.: Fast glacier flow – ice streams, surging, and tidewater glaciers, J. Geophys. Res.-Solid, 92, 8835–8841, 1987. 2688, 2699

Comiso, J. C.: Variability and trends in Antarctic surface temperatures from in situ and satellite infrared measurements, J. Climate, 13, 1674–1696, doi:10.1175/1520-0442(2000)013<1674:VATIAS>2.0.CO;2, 2000. 2698

Cook, C. P., van de Flierdt, T., Williams, T., Hemming, S. R., Iwai, M., Kobayashi, M., Jimenez-Espejo, F. J., Escutia, C., Jairo Gonzalez, J., Khim, B.-K., McKay, R. M., Passchier, S., Bohaty, S. M., Riesselman, C. R., Tauxe, L., Sugisaki, S., Lopez Galindo, A., Patterson, M. O., Sangiorgi, F., Pierce, E. L., and Brinkhuis, H.: Dynamic behaviour of the East Antarctic ice sheet during Pliocene warmth, Nat. Geosci., 6, 765–769, doi:10.1038/NGEO1889, 2013. 2687, 2696

den Ouden, M. A. G., Reijmer, C. H., Pohjola, V., van de Wal, R. S. W., Oerlemans, J., and Boot, W.: Stand-alone single-frequency GPS ice velocity observations on Nordenskiöldbreen, Svalbard, The Cryosphere, 4, 593–604, doi:10.5194/tc-4-593-2010, 2010. 2691

Deschamps, P., Durand, N., Bard, E., Hamelin, B., Camoin, G., Thomas, A. L., Henderson, G. M., Okuno, J., and Yokoyama, Y.: Ice-sheet collapse and sea-level rise at the Bolling warming 14 and 600 years ago, Nature, 483, 559–564, doi:10.1038/nature10902, 2012. 2687, 2688

Dowdeswell, J. A., Hamilton, G., and Hagen, J.: The duration of the active phase on surge-type glaciers: contrasts between Svalbard and other regions, J. Glaciol., 37, 388–400, 1991. 2691

Dowdeswell, J. A., Unwin, B., Nuttall, A. M., and Wingham, D. J.: Velocity structure, flow instability and mass flux on a large Arctic ice cap from satellite radar interferometry, Earth Planet. Sc. Lett., 167, 131–140, 1999. 2690, 2694, 2696

Dowdeswell, J. A., Ottesen, D., Evans, J., Cofaigh, C., and Anderson, J.: Submarine glacial landforms and rates of ice-stream collapse, Geology, 36, 819–822, 2008. 2690, 2694, 2697

TCD
8, 2685–2719, 2014

Dunse, T., Schuler, T. V., Hagen, J., Eiken, T., Brandt, O., and Høgda, K.: Recent fluctuations in the extent of the firn area of Austfonna, Svalbard, inferred from GPR, Ann. Glaciol., 50, 155–162, doi:10.3189/172756409787769780, 2009. 2692, 2702

Dunse, T., Greve, R., Schuler, T. V., and Hagen, J. O.: Permanent fast flow vs. cyclic surge behaviour: numerical simulations of the Austfonna ice cap, Svalbard, J. Glaciol., 57, 247–259, 2011. 2695, 2696

Dunse, T., Schuler, T. V., Hagen, J. O., and Reijmer, C. H.: Seasonal speed-up of two outlet glaciers of Austfonna, Svalbard, inferred from continuous GPS measurements, The Cryosphere, 6, 453–466, doi:10.5194/tc-6-453-2012, 2012. 2691, 2692, 2702, 2711

Gardner, A. S., Moholdt, G., Wouters, B., Wolken, G. J., Burgess, D. O., Sharp, M. J., Cogley, J. G., Braun, C., and Labine, C.: Sharply increased mass loss from glaciers and ice caps in the Canadian Arctic Archipelago, Nature, 473, 357–360, doi:10.1038/nature10089, 2011. 2686

Hamilton, G. S. and Dowdeswell, J. A.: Controls on glacier surging in Svalbard, J. Glaciol., 42, 157–168, 1996. 2689, 2696

Joughin, I. and Alley, R. B.: Stability of the West Antarctic ice sheet in a warming world, Nat. Geosci., 4, 506–513, doi:10.1038/NGEO1194, 2011. 2689, 2695, 2696

Joughin, I., Smith, B. E., Shean, D. E., and Floricioiu, D.: Brief Communication: Further summer speedup of Jakobshavn Isbræ, The Cryosphere, 8, 209–214, doi:10.5194/tc-8-209-2014, 2014. 2697

Kaser, G., Cogley, J. G., Dyurgerov, M. B., Meier, M. F., and Ohmura, A.: Mass balance of glaciers and ice caps: Consensus estimates for 1961–2004, Geophys. Res. Lett., 33, L19501, doi:10.1029/2006GL027511, 2006. 2686

Khan, S. A., Kjaer, K. H., Bevis, M., Bamber, J. L., Wahr, J., Kjeldsen, K. K., Bjork, A. A., Korsgaard, N. J., Stearns, L. A., van den Broeke, M. R., Liu, L., Larsen, N. K., and Muresan, I. S.: Sustained mass loss of the northeast Greenland ice sheet triggered by regional warming, Nature Climate Change, 4, 292–299, doi:10.1038/NCLIMATE2161, 2014. 2687, 2697

Lefauconnier, B. and Hagen, J.: Surging and Calving Glaciers in Eastern Svalbard, Norsk Polarinstitutt, Oslo and Norway, 1991. 2690, 2691

MacAyeal, D.: Binge/purge oscillations of the Laurentide Ice Sheet as a cause of the North Atlantic's Heinrich events, Paleoceanography, 8, 775–784, 1993. 2689

Meier, M. and Post, A.: Fast tidewater glaciers, J. Geophys. Res.-Solid, 92, 9051–9058, 1987. 2687

TCD
8, 2685–2719, 2014

Meierbachtol, T., Harper, J., and Humphrey, N.: Basal drainage system response to increasing surface melt on the Greenland ice sheet, Science, 341, 777–779, doi:10.1126/science.1235905, 2013. 2697

Moholdt, G. and Kääb, A.: A new DEM of the Austfonna ice cap by combining differential SAR interferometry with ICESat laser altimetry, Polar Res., 31, 18460, doi:10.3402/polar.v31i0.18460, 2012. 2691, 2699, 2701, 2711

Moholdt, G., Hagen, J. O., Eiken, T., and Schuler, T. V.: Geometric changes and mass balance of the Austfonna ice cap, Svalbard, The Cryosphere, 4, 21–34, doi:10.5194/tc-4-21-2010, 2010a. 2690

Moholdt, G., Nuth, C., Hagen, J. O., and Kohler, J.: Recent elevation changes of Svalbard glaciers derived from ICESat laser altimetry, Remote Sens. Environ., 114, 2756–2767, 2010b. 2694, 2697

Mouginot, J., Rignot, E., and Scheuchl, B.: Sustained increase in ice discharge from the Amundsen Sea Embayment, West Antarctica, from 1973 to 2013, Geophys. Res. Lett., 41, 1576–1584, doi:10.1002/2013GL059069, 2014. 2687

Nick, F. M., Vieli, A., Andersen, M. L., Joughin, I., Payne, A., Edwards, T. L., Pattyn, F., and van de Wal, R. S. W.: Future sea-level rise from Greenland's main outlet glaciers in a warming climate, Nature, 497, 235–238, doi:10.1038/nature12068, 2013. 2688, 2698

Pattyn, F.: Antarctic subglacial conditions inferred from a hybrid ice sheet/ice stream model, Earth Planet. Sc. Lett., 295, 451–461, doi:10.1016/j.epsl.2010.04.025, 2010. 2696

Pfeffer, W. T.: A simple mechanism for irreversible tidewater glacier retreat, J. Geophys. Res., 112, F03S25, doi:10.1029/2006JF000590, 2007. 2687

Phillips, T., Rajaram, H., and Steffen, K.: Cryo-hydrologic warming: a potential mechanism for rapid thermal response of ice sheets, Geophys. Res. Lett., 37, L20503, doi:10.1029/2010GL044397, 2010. 2688

Phillips, T., Rajaram, H., Colgan, W., Steffen, K., and Abdalati, W.: Evaluation of cryo-hydrologic warming as an explanation for increased ice velocities in the wet snow zone, Sermeq Avannarleq, West Greenland, J. Geophys. Res.-Earth, 118, 1241–1256, doi:10.1002/jgrf.20079, 2013. 2697

Raymond, C.: How do glaciers surge – a review, J. Geophys. Res.-Solid, 92, 9121–9134, 1987. 2689

TCD
8, 2685–2719, 2014

Robinson, P. and Dowdeswell, J.: Submarine landforms and the behavior of a surging ice cap since the last glacial maximum: The open-marine setting of eastern Austfonna and Svalbard, Mar. Geol., 286, 82–94, doi:10.1016/j.margeo.2011.06.004, 2011. 2691

Schoof, C.: Ice-sheet acceleration driven by melt supply variability, Nature, 468, 803–806, doi:10.1038/nature09618, 2010. 2688, 2695

Schuler, T. V., Dunse, T., Østby, T. I., and Hagen, J. O.: Meteorological conditions on an Arctic ice cap – 8 years of automatic weather station data from Austfonna, Svalbard. Int. J. Climatol., 34, 2047–2058, doi:10.1002/joc.3821, 2014. 2692

Shannon, S. R., Payne, A. J., Bartholomew, I. D., van den Broeke, M. R., Edwards, T. L., Fettweis, X., Gagliardini, O., Gillet-Chaulet, F., Goelzer, H., Hoffman, M. J., Huybrechts, P., Mair, D. W. F., Nienow, P. W., Perego, M., Price, S. F., Smeets, C. J. P. P., Sole, A. J., van de Wal, R. S. W., and Zwinger, T.: Enhanced basal lubrication and the contribution of the Greenland ice sheet to future sea-level rise, P. Natl. Acad. Sci. USA, 110, 14156–14161, doi:10.1073/pnas.1212647110, 2013. 2688, 2698

Shepherd, A., Ivins, E. R., Geruo, A., Barletta, V. R., Bentley, M. J., Bettadpur, S., Briggs, K. H., Bromwich, D. H., Forsberg, R., Galin, N., Horwath, M., Jacobs, S., Joughin, I., King, M. A., Lenaerts, J. T. M., Li, J., Ligtenberg, S. R. M., Luckman, A., Luthcke, S. B., McMillan, M., Meister, R., Milne, G., Mouginot, J., Muir, A., Nicolas, J. P., Paden, J., Payne, A. J., Pritchard, H., Rignot, E., Rott, H., Sorensen, L. S., Scambos, T. A., Scheuchl, B., Schrama, E. J. O., Smith, B., Sundal, A. V., van Angelen, J. H., van de Berg, W. J., van den Broeke, M. R., Vaughan, D. G., Velicogna, I., Wahr, J., Whitehouse, P. L., Wingham, D. J., Yi, D., Young, D., and Zwally, H. J.: A reconciled estimate of ice-sheet mass balance, Science, 338, 1183–1189, doi:10.1126/science.1228102, 2012. 2686, 2687

Stocker, T. F., Qin, D., Plattner, G.-K., Alexander, L. V., Allen, S. K., Bindoff, N. L., Bréon, F.-M., Church, J. A., Cubasch, U., Emori, S., Forster, P., Friedlingstein, P., Gillett, N., Gregory, J. M., Hartmann, D. L., Jansen, E., Kirtman, B., Knutti, R., Krishna Kumar, K., Lemke, P., Marotzke, J., Masson-Delmotte, V., Meehl, G. A., Mokhov, I. I., Piao, S., Ramaswamy, V., Randall, D., Rhein, M., Rojas, M., Sabine, C., Shindell, D., Talley, L. D., Vaughan, D. G., and Xie, S.-P.: Technical Summary, in: Climate Change 2013: The Physical Science Basis. Contribution of Working Group I to the Fifth Assessment Report of the Intergovernmental Panel on Climate Change, edited by: Stocker, T. F., Qin, D., Plattner, G.-K., Tignor, M., Allen, S. K., Boschung, J., Nauels, A., Xia, Y., Bex, V., and Midgley P. M., Cambridge University Press, Cambridge, United Kingdom and New York, NY, USA, 2013. 2687, 2698

TCD
8, 2685–2719, 2014

Strozzi, T., Luckman, A., Murray, T., Wegmüller, U., and Werner, C. L.: Glacier motion estimation using SAR offset-tracking procedures, IEEE T. Geosci. Remote, 40, 2384–2391, 2002. 2691, 2698

Tedesco, M., Fettweis, X., Mote, T., Wahr, J., Alexander, P., Box, J. E., and Wouters, B.: Evidence and analysis of 2012 Greenland records from spaceborne observations, a regional climate model and reanalysis data, The Cryosphere, 7, 615–630, doi:10.5194/tc-7-615-2013, 2013. 2686

Tulaczyk, S., Kamb, W. B., and Engelhardt, H. F.: Basal mechanics of Ice Stream B and West Antarctica 2. Undrained plastic bed model, J. Geophys. Res.-Sol. Ea., 105, 483–494, 2000. 2689, 2696

Zagorodnov, V., Sinkevich, S., and Arkhipov, S.: Ice core express-analysis for structure and thermal regime studies of Austfonna, Data of Glaciological Studies, 66, 149–158, 1989 (in Russian with English summary). 2690

Zwally, H. J., Abdalati, W., Herring, T., Larson, K., Saba, J., and Steffen, K.: Surface melt-induced acceleration of Greenland ice-sheet flow, Science, 297, 218–222, 2002. 2688

TCD
8, 2685–2719, 2014

Table 1. Estimate of calving flux components and total calving flux over the TSX observation period from 19 April 2012 to 9 May 2013.

Calving Flux components	(Gt)	(Gt a^{-1})
Ice flux, Q_{fg}	8.3 ± 2.8	7.8 ± 2.7
Terminus change, Q_t	3.8 ± 1.2	3.6 ± 1.1
Terminus-seawater displacement, Q_{tsd}	3.2 ± 1.1	3.0 ± 1.0
Total calving flux		
Mb perspective, $Q_{mb} = Q_{fg} - Q_t$	4.4 ± 1.6	4.2 ± 1.5
SLR perspective, $Q_{sl} = Q_{mb} + Q_{tsd}$	7.6 ± 3.9	7.2 ± 2.6

TCD
8, 2685–2719, 2014

Table A1. TerraSAR-X acquisitions of Basin-3 and repeat-pass period and maximum velocities of inferred velocity maps.

ID of period	Repeat pass period (days)	Start and end-date (dd mm yyyy)	Maximum velocity ($m\,d^{-1}$)
t_1	11	19 Apr 2012–30 Apr 2012	4.5
t_2	11	30 Apr 2012–11 May 2012	4.5
t_3	88	30 Apr 2012–7 Aug 2012	4.5
t_4	11	7 Aug 2012–18 Aug 2012	6.4
t_5	11	18 Aug 2012–29 Aug 2012	6.8
t_6	44	29 Aug 2012–12 Oct 2012	8.4
t_7	11	12 Oct 2012–23 Oct 2012	13.6
t_8	11	23 Oct 2012–3 Nov 2012	13.6
t_9	22	3 Nov 2012–25 Nov 2012	15.9
t_{10}	11	25 Nov 2012–6 Dec 2012	18.2
t_{11}	22	6 Dec 2012–28 Dec 2012	18.4
t_{12}	11	28 Dec 2012–8 Jan 2013	20.0
t_{13}	22	8 Jan 2013–30 Jan 2013	18.6
t_{14}	11	30 Jan 2013–10 Feb 2013	18.6
t_{15}	22	10 Feb 2013–4 Mar 2013	17.5
t_{16}	11	4 Mar 2013–15 Mar 2013	17.3
t_{17}	22	15 Mar 2013–6 Apr 2013	16.1
t_{18}	11	6 Apr 2013–17 Apr 2013	16.4
t_{19}	22	17 Apr 2013–9 May 2013	15.2
t_{20}	11	16 Aug 2013–27 Aug 2013	15.5
t_{21}	11	12 Nov 2013–23 Nov 2013	12.5

TCD
8, 2685–2719, 2014

Table B1. Calving flux input variables – values, sources and uncertainties.

Variable	Value/Source	Uncertainty	Explanation
zs_{fg}	40 m (constant)	±30 m	The chosen values allow for elevations from flotation height of 10 m as lower limit and mean DEM height of 67 m as upper limit. The DEM originates from prior to surge initiation. GPS data since 2008 indicates extensional flow, and hence, dynamic thinning.
zb_{fg}	Local bedrock map values along fluxgate	±30 m	Twice the accuracy in ice thickness measurement of ±15 m used to derive the bedrock map (Dunse et al., 2012), thereby accounting for uncertainties introduced by gridding of spatial inhomogeneous measurements.
H_{fg}	$zs_{fg} - zb_{fg}$	±42 m	RSS of errors in zs_{fg} and zb_{fg}.
zs_t	30 m (constant)	±20 m	Allows for calving front heights down to flotation and significantly larger than typical front height of 30 m (Moholdt and Kääb, 2012).
zb_t	−87 m (constant)	±30 m	Value represents the mean bedrock elevation within the observed range in front position with an uncertainty analogue to the one of zb_{fg}.
H_t	$zs_t - zb_t$	±36 m	RSS of errors in zs_t and zb_t.
v_{fg}	Local value from TSX velocity maps	±0.37 m d^{-1} (0.42 for t_3 and 0.44 for t_6)	Uncertainty based on standard deviation (std) of TSX and GPS velocities, yielding a 0.37 m d^{-1}; for the long repeat cycles t_3 and t_6, additional uncertainty is added based on a comparison of the available data (51 and 46 % coverage) and reconstructed velocity profile, resulting in a std of 0.21 and 0.25 m d^{-1}.
Front position	2 m resolution TSX backscatter image	±8 m (4 pixels)	Digitizing error of calving front position results in uncertainty of ΔA_{cf}, determined by RSS of deviation from minimum and maximum extent of A_{cf} at times $t_{i,start}$ and $t_{i,start}$.

TCD
8, 2685–2719, 2014

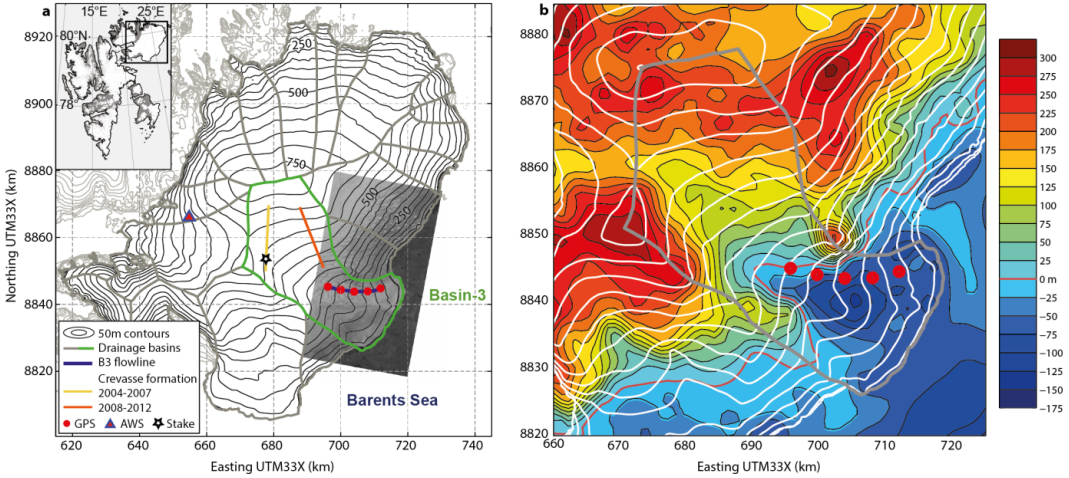

Figure 1. Surface and bedrock topography of Austfonna/Basin-3. **(a)** Surface elevation contours at 50 m interval (solid black), overlain on a TerraSAR-X backscatter image (30 April 2012). The insert provides the ice cap's location within the Svalbard archipelago. Drainage basins are outlined in solid grey, solid green for Basin-3. Position of five GPS receivers and one stake on Basin-3, as well as the automatic weather station (AWS) are marked. Repeat-GPR profiling revealed crevasse formation in upper reaches of Basin-3 between 2004–2007 and 2008–2012 (Appendix D). **(b)** Bedrock contours (black, color-filled) are at 25 m intervals, with the bedrock sea-level contour highlighted in red and 50 m surface elevation contours superimposed (white).

TCD
8, 2685–2719, 2014

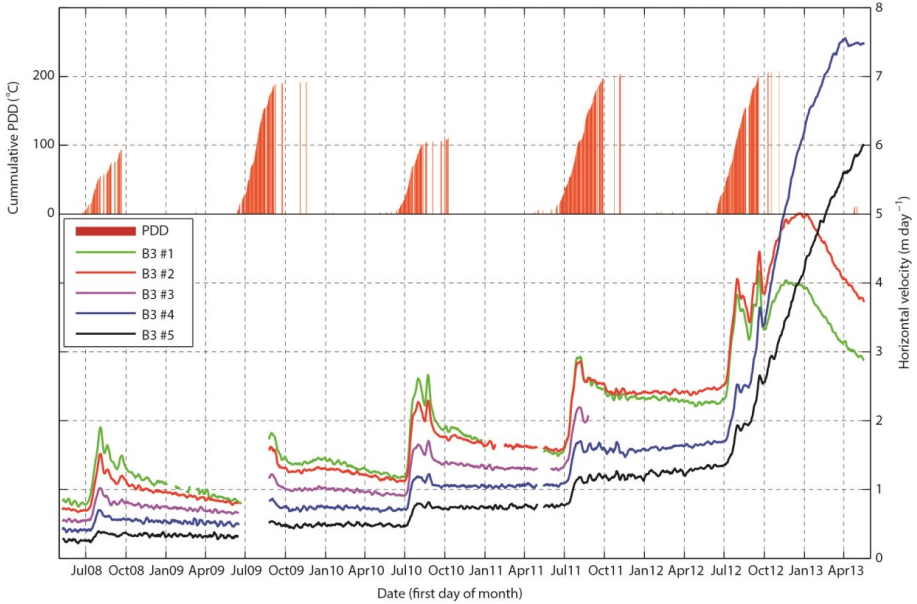

Figure 2. Flow velocities along the centreline of the ice stream of Basin-3, Austfonna, between May 2008 and May 2013. GPS stations are numbered from 1 at lowest to 5 at highest elevation (Fig. 1). Red bars (upper panel) indicate potential melt days and cumulative positive degree days (PDD) for each summer, inferred from the temperature record of an automatic weather station.

TCD
8, 2685–2719, 2014

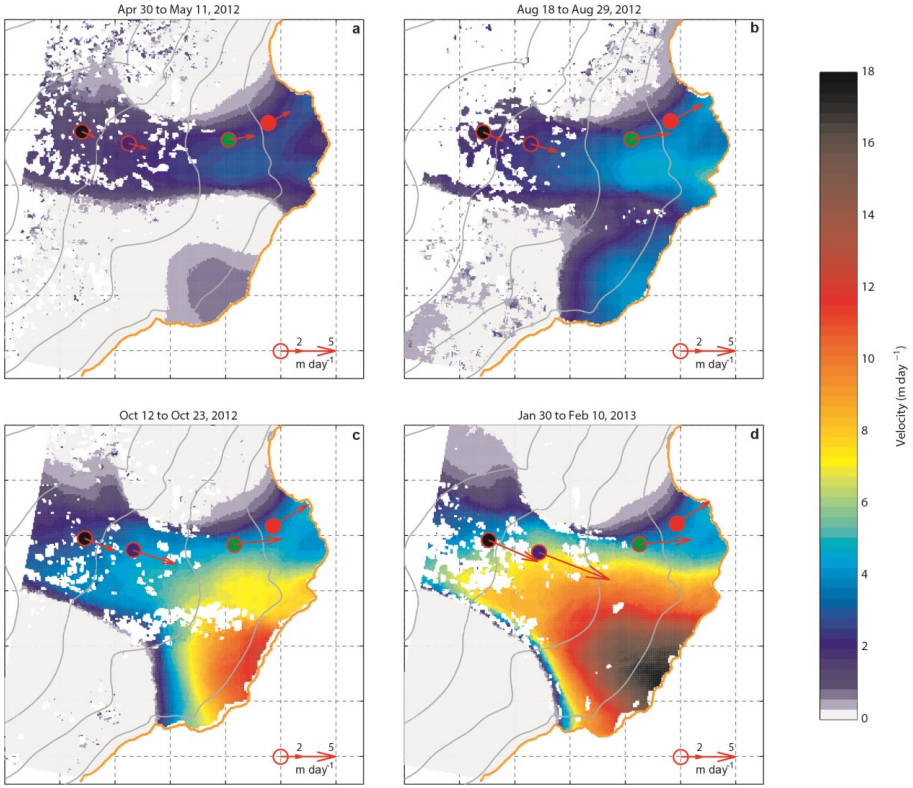

Figure 3. Surface velocity fields of Basin-3, Austfonna, derived from TerraSAR-X feature tracking; **(a)** April/May 2012; **(b)** August; **(c)** October; and **(d)** January/February 2013. Red circles represent mean position of GPS receivers over the particular repeat-pass period, fillcolor according to color-coding of receivers in Fig. 2. The red arrows indicate associated GPS velocity vectors. Glacier elevation contours plotted in grey at 100 m intervals, front position at time of repeat pass in orange.

TCD
8, 2685–2719, 2014

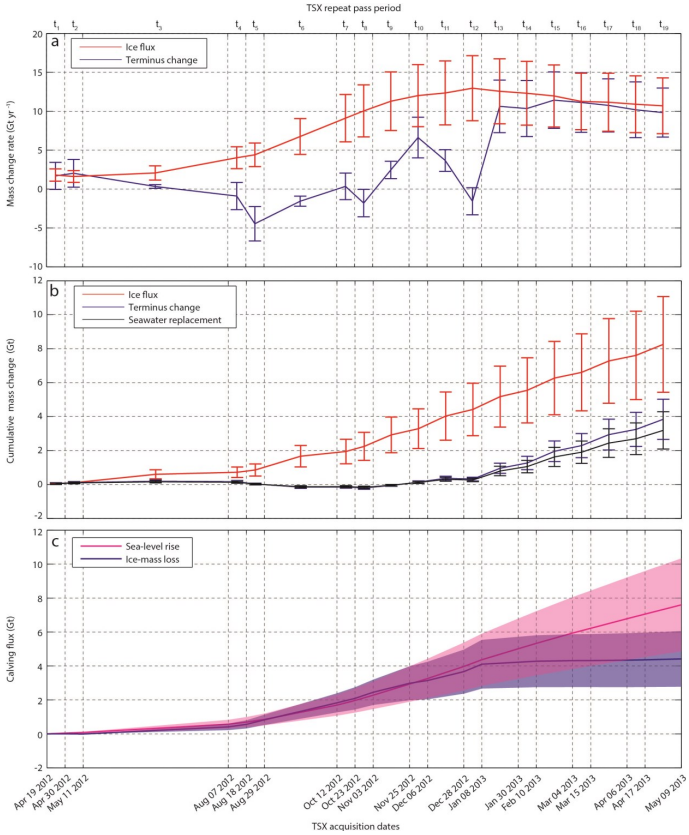

Figure 4. Calving-flux from Basin-3, Austfonna, April 2012 to May 2013. Calving components are expressed in terms of the instantaneous **(a)** and cumulative mass change **(b)** and allocated to the effect on glacier mass balance and sea-level (**c**; see Sect. 4.3). Whiskers **(a, b)** indicate uncertainty bounds calculated using propagation-of-uncertainty analysis and shaded areas **(c)** upper and lower bounds given maximum or minimum ice thickness.

TCD
8, 2685–2719, 2014

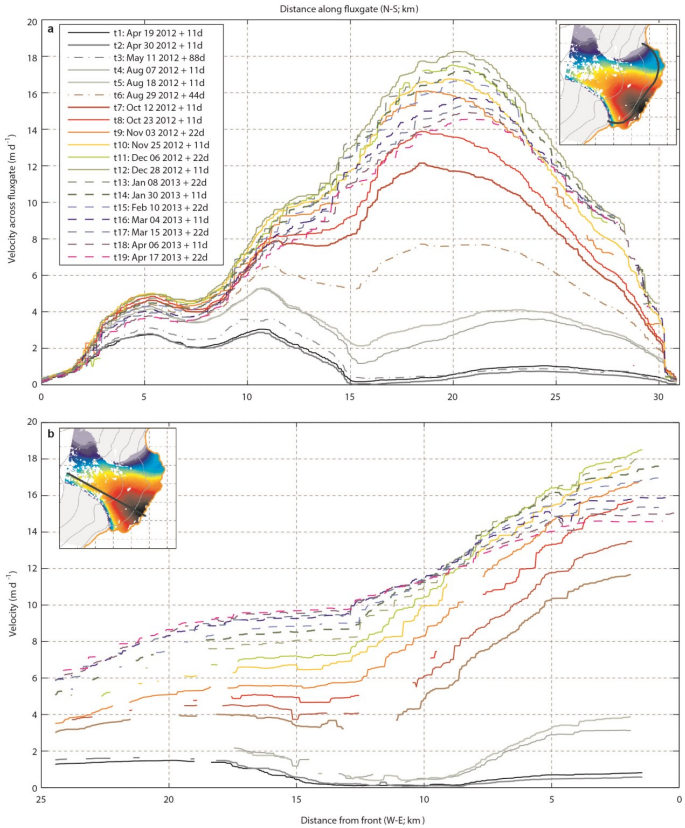

Figure A1. Evolution of ice-flow velocities across a calving fluxgate **(a)** and along a central flowline of Basin-3 **(b)**. Velocity profiles extracted from TerraSAR-X velocity maps April 2012 to May 2013 and median filtered to remove outliers. The insert shows the location of the profiles overlain onto the velocity map of t_{14}. Fluxgate velocities are used to compute the calving ice flux. Velocities for long repeat passes t_3 and t_6 have been constructed as described in B2.

TCD
8, 2685–2719, 2014

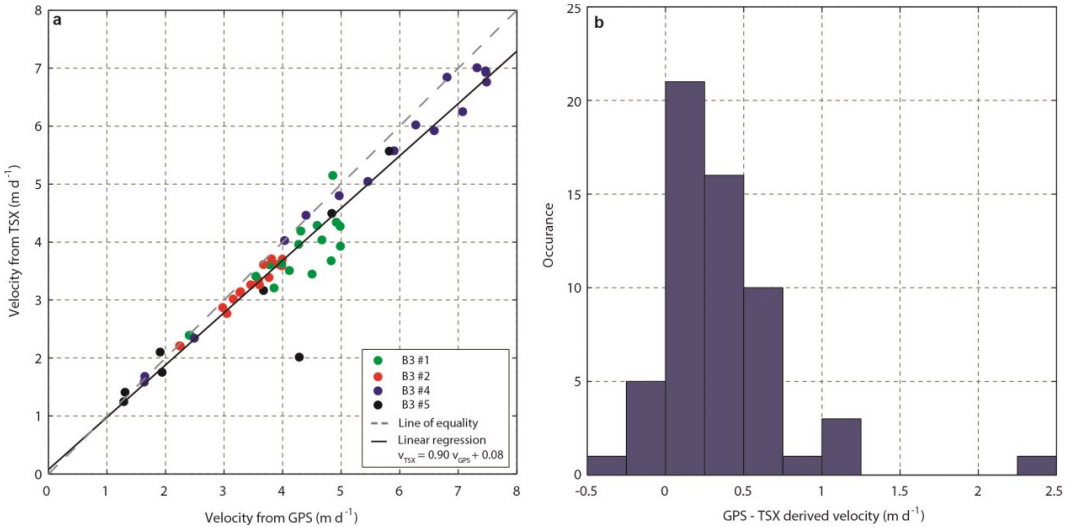

Figure A2. Comparison of TSX and GPS velocities at GPS locations and for each repeat-pass period. **(a)** Linear regression (solid black; R^2 = 0.94) predicts 94 % of the variance in TSX velocities (0.14 m d^{-1}). **(b)** TSX velocities typically slightly underestimate local (sub-pixel scale) velocities measured at the GPS stations by 0.3 m d^{-1}.

TCD
8, 2685–2719, 2014

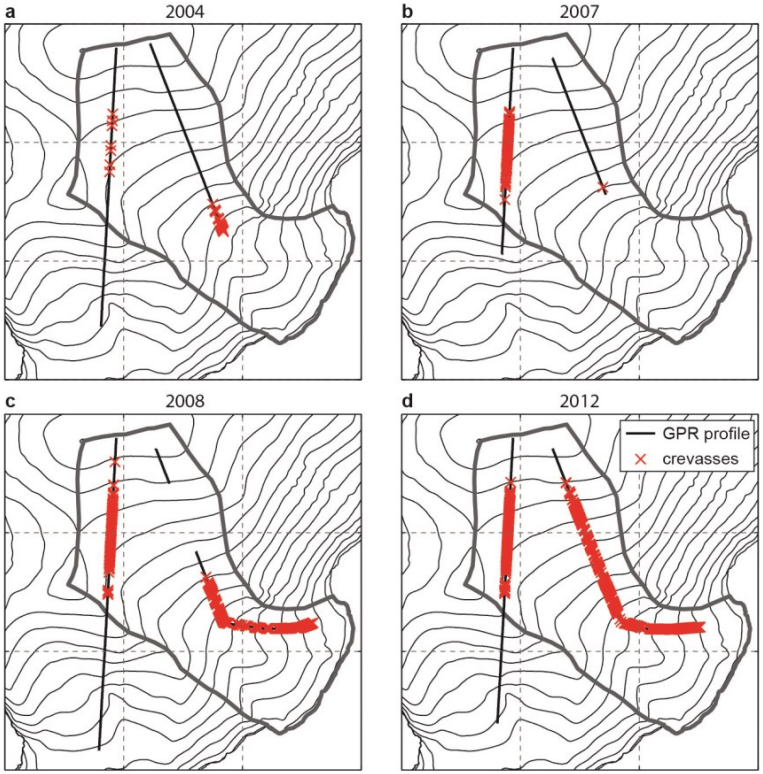

Figure C1. Crevasse formation on upper Basin-3 in 2004–2012, inferred from GPR. GPR profiles are plotted in solid black, detected crevasses are marked by a red cross. The outline of Basin-3 is shown in dark grey.

TCD
8, 2685–2719, 2014

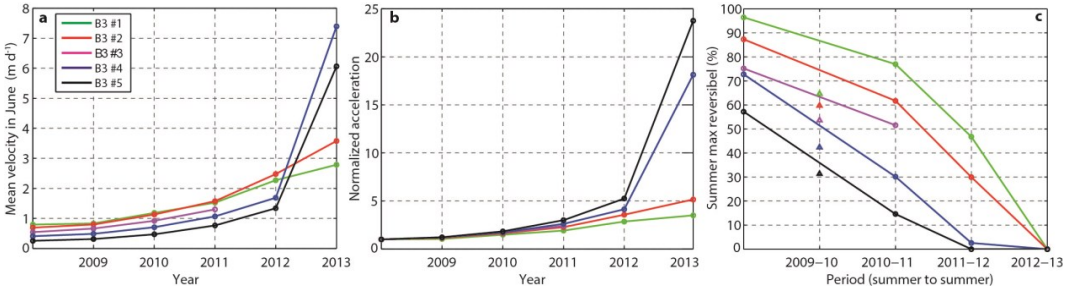

Figure D1. GPS-velocity evolution along a central flowline of Basin-3; **(a)** annual velocity minimum defined as the mean value in June 2008 to 2013 and **(b)** normalized to mean-June velocity 2008; **(c)** reversibility of summer speed-up defined as the ratio of the velocity increase from pre-summer minimum (mean June) to maximum summer velocity and subsequent velocity decrease to pre-summer velocity of subsequent year. In 2009, summer maximum velocities were not captured due to GPS power loss. The triangles only indicate a minimum estimate for 2009–2010, based on elevated late-summer velocities measured after maintenance of GPS receivers in end of August.

TCD
8, 2685–2719, 2014